Extremely large magnetoresistance and Shubnikov–de Haas oscillations in the topological nodal-line semimetal ZrP_2

Xingze Dai, Zhihao Li, Yongkang Xu, Yafeng Deng, Yilin Zhang, Pengfei Yan, Jin Wang, Shuanghai Wang, Kun He, Yao Li, Yongbing Xu, and Liang He*

State Key Laboratory of Spintronics Devices and Technologies, School of Electronic Science and Engineering, Nanjing University, Nanjing 210023, China

(Received 13 November 2023; accepted 10 April 2024; published 30 April 2024)

The topological semimetals have been the research focus of condensed-matter physics, materials science, and spintronics in recent decades. Here, we report the magnetoelectric transport properties of the topological nodal-line semimetal ZrP_2. A clear magnetic-field induced metal-to-insulator transition is observed, and a resistivity plateau appears as the temperature drops to 15 K. An extremely large magnetoresistance of 15 000% obtained at low temperatures confirms Kohler's rule, which is ascribed to the electron-hole compensation. The beating patterns of Shubnikov–de Haas quantum oscillations are also observed below 10 K, which mainly stems from the superposition of two oscillations from electron and hole pockets, which is also consistent with the theoretical calculations. These findings provide a candidate material for the study of topological nodal-line semimetal in exploring physical properties and topological electronics.

DOI: 10.1103/PhysRevB.109.165155

I. INTRODUCTION

Recently, topological semimetals have stimulated intensive research interest in the topological condensed-matter physics and spintronics due to their unique energy band structure and unconventional transport properties, such as Dirac cone [1,2], Fermi arc surface states [1], extremely large magnetoresistance (MR) [3–5], ultrahigh mobility [3,6–8], quantum Hall effect [9,10], Shubnikov–de Haas (SdH) quantum oscillations [3,11], etc. According to energy band structure, topological semimetals can be broadly classified into Dirac semimetals (DSMs), Weyl semimetals (WSMs), and nodal-line semimetals (NLSMs). In DSMs, the energy bands cross linearly near the Femi level E_F in k space, and the crossing point is called a Dirac node with fourfold degeneracy, which is protected by time-reversal symmetry and spatial-inversion symmetry [12,13]. If one or both of the time-reversal symmetry and spatial-inversion symmetry are broken, a Dirac node is split into two double-degenerated nodes. The double-degenerated node is called a Weyl node, and the corresponding semimetal is called a WSM [5,13]. In contrast to DSMs and WSMs, the energy bands of the NLSMs cross at a one-dimensional line in k space (termed as nodal line), and the nodal line can be a closed loop, an open line, or an interlinked chain. [5,13]. Like DSMs and WSMs, the NLSMs also have unique surface states, the so-called drumhead surface states, which are not topologically protected; a small perturbation to the surface can destroy the drumhead surface states [14]. The topological semimetals provide a broad platform for exploring novel physical properties and topological fermions.

The exotic and rich physical properties have been theoretically predicted and experimentally demonstrated in some topological semimetals. The most famous examples are the DSMs and WSMs, in which the Dirac cones and Fermi arcs have been discovered in the three-dimensional Dirac semimetal Na_3Bi, Cd_3As_2, and TaAs family by the first-principles calculations and angle-resolved photoemission spectroscopy (ARPES) [2,15,16]. The chiral anomaly effect, extremely large MR, SdH quantum oscillations, and ultrahigh mobility have also been observed in TaAs [17–19], WTe_2 [4], NbP [3], and WP_2 [20]. The DSMs and WSMs have been extensively studied and show excellent properties in the field of photodetection [21–26], photovoltaic effect [27], photothermoelectric effect [28], terahertz emission [29,30], etc. However, the NLSMs has not been adequately studied. So far, only a few candidate materials have been identified to be NLSMs, such as CaP_3 family [31], ZrSiTe family [32], Nb_3SiTe_6 family [33], etc. Recently, the transition-metal dipnictides HfP_2 and ZrP_2 have been identified to be NLSMs by the first-principles calculations and ARPES [5,34]. However, the transport properties are still unclear. Therefore, it is meaningful to comprehensively investigate the magnetoelectric transport properties for topological semimetal ZrP_2.

In this work, after [35] synthesizing the high-quality single-crystal ZrP_2 by chemical vapor transport (CVT) method, its magnetoelectric transport properties have been investigated. At low temperatures, the magnetic-field induced metal-to-insulator transition and resistivity plateau with an extremely large unsaturated magnetoresistance (MR) of 1.5×10^4 % are obtained. More importantly, the beating patterns of SdH quantum oscillations are clearly observed, which mainly stem from the superposition of the quantum oscillations of the electron and hole pockets. Besides, an unusual SdH quantum oscillation due to the Zeeman effect is also

*heliang@nju.edu.cn

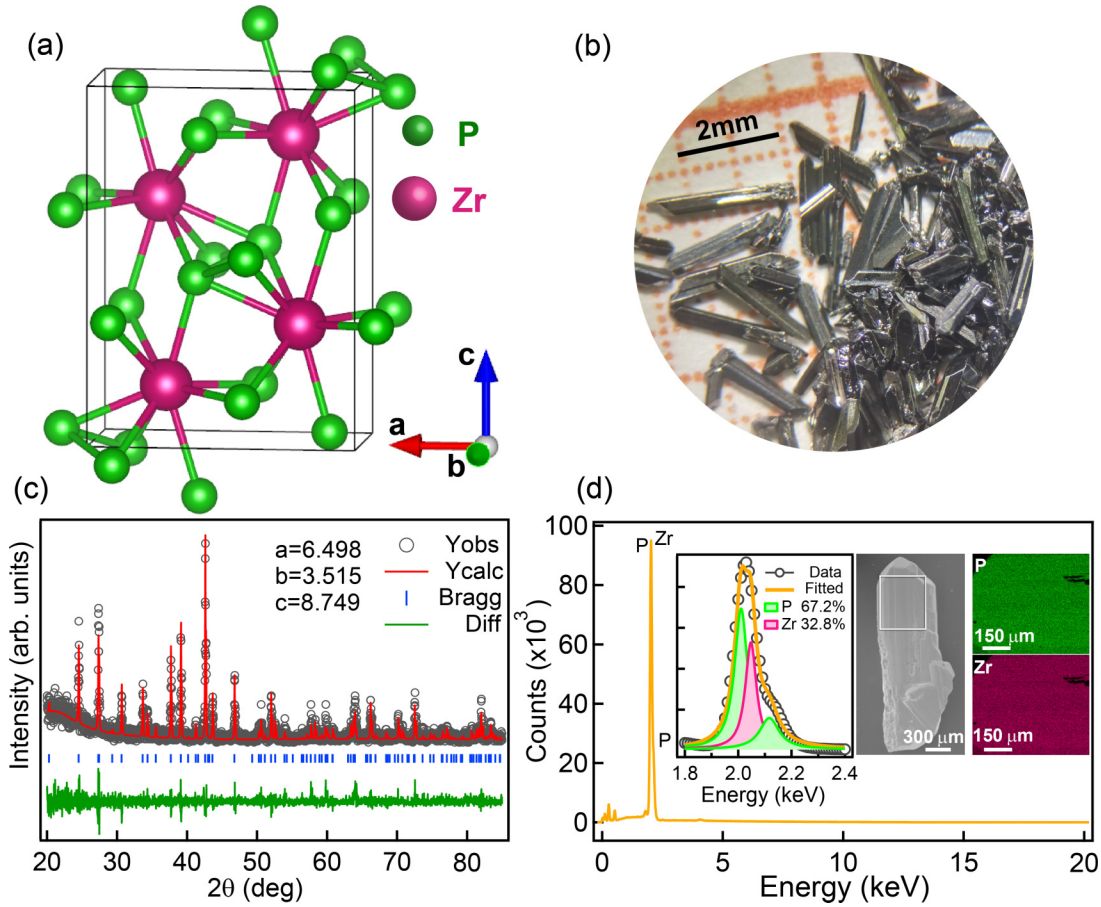

FIG. 1. (a) The crystal structure of ZrP_2. (b) The image of the single-crystal ZrP_2 samples. (c) Powder XRD and the Rietveld refinement results. (d) The morphology and elemental distribution of the ZrP_2.

observed at 1.6 K. These findings provide a candidate material to explore condensed-matter physics and topological electronics.

II. EXPERIMENTAL METHODS

High-quality single-crystal ZrP_2 is grown via the CVT method using I_2 as the transport agent. First, the polycrystalline ZrP_2 intermediate products are prepared by sintering a stoichiometric mixture of zirconium powder (Alfa Aesar, 99.99%) and red phosphorus (Alfa Aesar, 99.999%) in an evacuated silica ampoule at 800 °C for 6 days. Subsequently, the polycrystalline ZrP_2 powder is loaded together with 5-mg/cm^3 iodine in a silica ampoule. The ampoule is evacuated and sealed under vacuum, and loaded into a horizontal tube furnace for 2 weeks, in which the temperature of the polycrystalline ZrP_2 powder is kept at 760 °C (source) and the temperature of the other end is kept at 810 °C (sink) [5]. Then, the tube furnace is naturally cooled down to room temperature. The needlelike single crystals with a size of $5 \times 0.3 \times 0.2\,\mathrm{mm}^3$ are obtained in the sink end. The x-ray-diffraction (XRD) pattern of ZrP_2 powder confirms its $PbCl_2$-type orthorhombic structure. The energy-dispersive x-ray (EDX) is used to determine the atomic ratio of the sample. A conventional four-probe device is prepared by attaching Au wires of 25-μm diameter to the sample with Epotek H20E silver epoxy. Transport measurements are performed using a cryogenic system (TeslatronPT, Oxford), in which the temperature can be cooled down to 1.6 K with a magnetic field up to 14 T. A Keithley 6221 current source is used to apply an ac current to the device. The voltage signals of the device are collected via the SR830 and OE1022D DSP lock-in amplifier.

III. RESULTS AND DISCUSSION

The ZrP_2 crystal belongs to the nonsymmorphic space group *Pnma* (No. 64) with the $PbCl_2$-type crystal structure [5,36,37], in which the Zr atoms are surrounded by nine P atoms in the form of a tricapped triangular prism, while partial P atoms are connected to one-dimensional infinite zigzag chains along the *b* axis, indicating a covalent bonding interaction as shown in Fig. 1(a). Figure 1(b) shows the needlelike single-crystal ZrP_2 samples grown by the CVT method. The powder XRD pattern is used to determine the crystal structure and quality. The Rietveld refinement results reveal that no obvious impurity phases can be detected, as shown in Fig. 1(c). The obtained lattice parameters of $a = 6.498$ Å, $b = 3.515$ Å, and $c = 8.749$ Å are in good agreement with previous reports [5,36]. Figure 1(d) demonstrates the evenly distributed elements in the sample by the Scanning Electron Microscope (SEM)–EDX measurement. And, the atomic ratio is obtained by fitting the energy-dispersive x-ray spectrome-

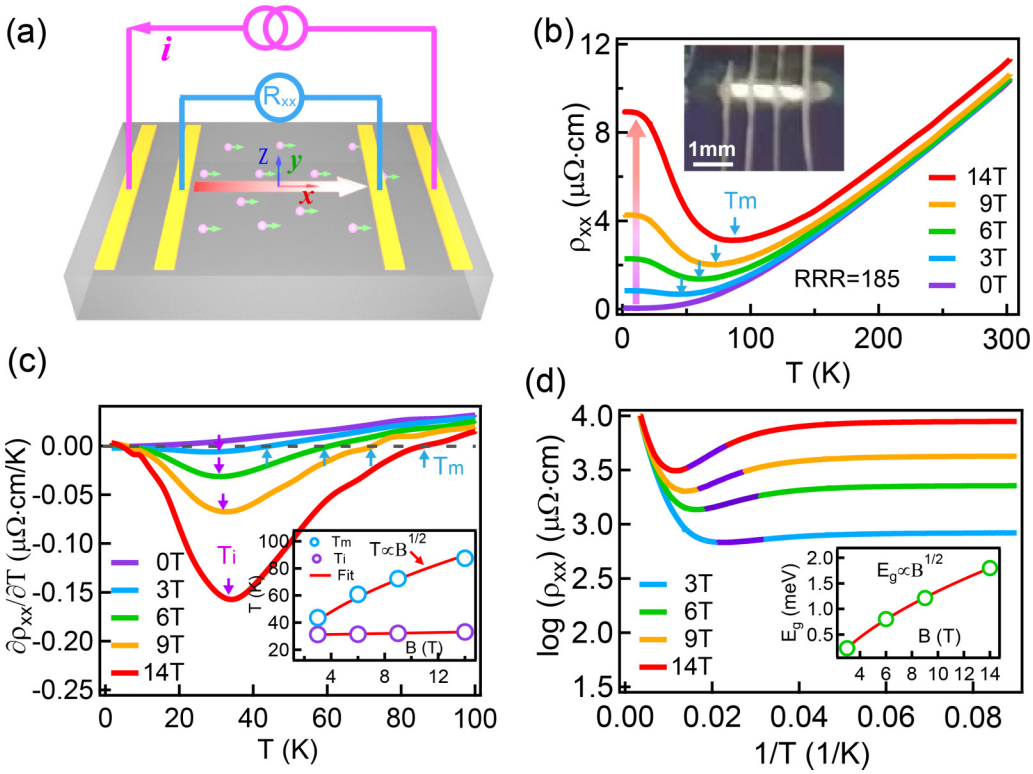

FIG. 2. (a) Schematic diagram of the resistivity measurement. (b) Temperature- dependent resistivity at various magnetic fields of 0, 3, 6, 9, and 14 T. A metal-to-insulator transition is present, induced by the magnetic field. The inset shows the image of the resistivity measurement. (c) The temperature dependence of the derivative $\partial\rho_{xx}/\partial T$ extracted from (b). The inset shows the T_m and T_i as a function of the field, where the red lines are the results of the $T \propto B^{1/2}$ and linear fitted, respectively. (d) The $\log(\rho_{xx})$ plotted as a function of T^{-1}. The purple solid lines exhibit the linearly fitted results for the Arrhenius plots, which give an activation energy of the effective band gap E_g. The inset shows the field-dependent E_g, and the red solid line is the curve fitted with $E_g \propto \mathrm{B}^{1/2}$.

try. The above results indicate that a high-quality ZrP_2 sample has been successfully grown by the CVT method.

Figure 2(a) exhibits a schematic diagram of the resistivity measurement with the conventional four-probe method. The temperature-dependent resistivity curves at various magnetic fields of 0, 3, 6, 9, and 14 T are summarized in Fig. 2(b), in which the direction of the magnetic field is along the z axis and normal to the current. In Fig. 2(b), the purple curve ($B = 0\,\mathrm{T}$) shows a metallic behavior as the temperature drops from 300 to 1.6 K. And, a high residual-resistivity ratio (RRR = 185) is obtained, which indicates high sample quality [38]. By applying an external magnetic field, a magnetic-field induced metal-to-insulator transition is observed. Interestingly, the resistivity plateau appears as the temperature cools down to 15 K. A similar resistivity plateau is also observed in the topological insulator Bi_2Se_3 [39,40] and Kondo insulator SmB_6 [41], which are attributed to topological surface states protected by the time-reversal symmetry. However, in our case, the time-reversal symmetry was broken due to the existence of external magnetic field. Thus, the resistivity plateau is ascribed to field-induced metal-to-insulator transition or Kohler's rule. Such resistivity plateaus are also observed in topological semimetals LaSb [42], WTe_2 [43], and $NbAs_2$ [44].

Figure 2(c) shows that the derivative $\partial\rho_{xx}/\partial T$ as a function of temperature T at various magnetic fields. At $B \geqslant 3$ T, a clear drop is seen and becomes more prominent for larger magnetic field B. The temperature at which the resistivity acquires minimum is defined as T_m, where $\partial\rho_{xx}/\partial T = 0$. The temperature of the valley T_i is defined by the inflection point, where $\partial^2\rho_{xx}/\partial T^2 = 0$. The T_m and T_i are summarized in the inset of Fig. 2(c). As shown in the figure, the T_i stays unchanged but the T_m increases monotonically with the magnetic field and satisfies the $T_m \propto B^v$ -type relation, where v has a value $\sim 1/2$. The same behaviors are also observed in other topological semimetals, such as graphite, Bi, and WTe_2 due to the Fermi-liquid state and quantum phase transition [45–48].

Considering the thermal transport at low temperatures, the energy gap E_g is estimated using the Arrhenius plot, $\rho_T = \rho_0 \exp(E_g/k_B T)$ for $T < T_m$. The $\log(\rho_{xx})$ are plotted as a function of T^{-1}, shown in Fig. 2(d). The gap E_g is plotted as a function of magnetic field B in the inset of Fig. 2(d), where the $E_g \propto B^{1/2}$. This is consistent with the gap opening due to the Landau-level quantization of relativistic Dirac electrons by the magnetic field [49].

The magnetic-field dependent MR is also investigated as shown in Fig. 3(a), where the $\mathrm{MR} = (\rho_{B-}\rho_0)/\rho_0 \times 100\%$ is the change in resistance with the magnetic field applied along the z axis and perpendicular to the current direction. The extremely large MR of the order of $10^4\%$ is obtained at low temperatures, which is comparable to that observed in previous reports [5]. The MR decreases to about 90% at 150 K and 14 T. The MR can be fitted by $\mathrm{MR} = a + bB^c$, with $c = 1.8$ in Fig. 3(b).

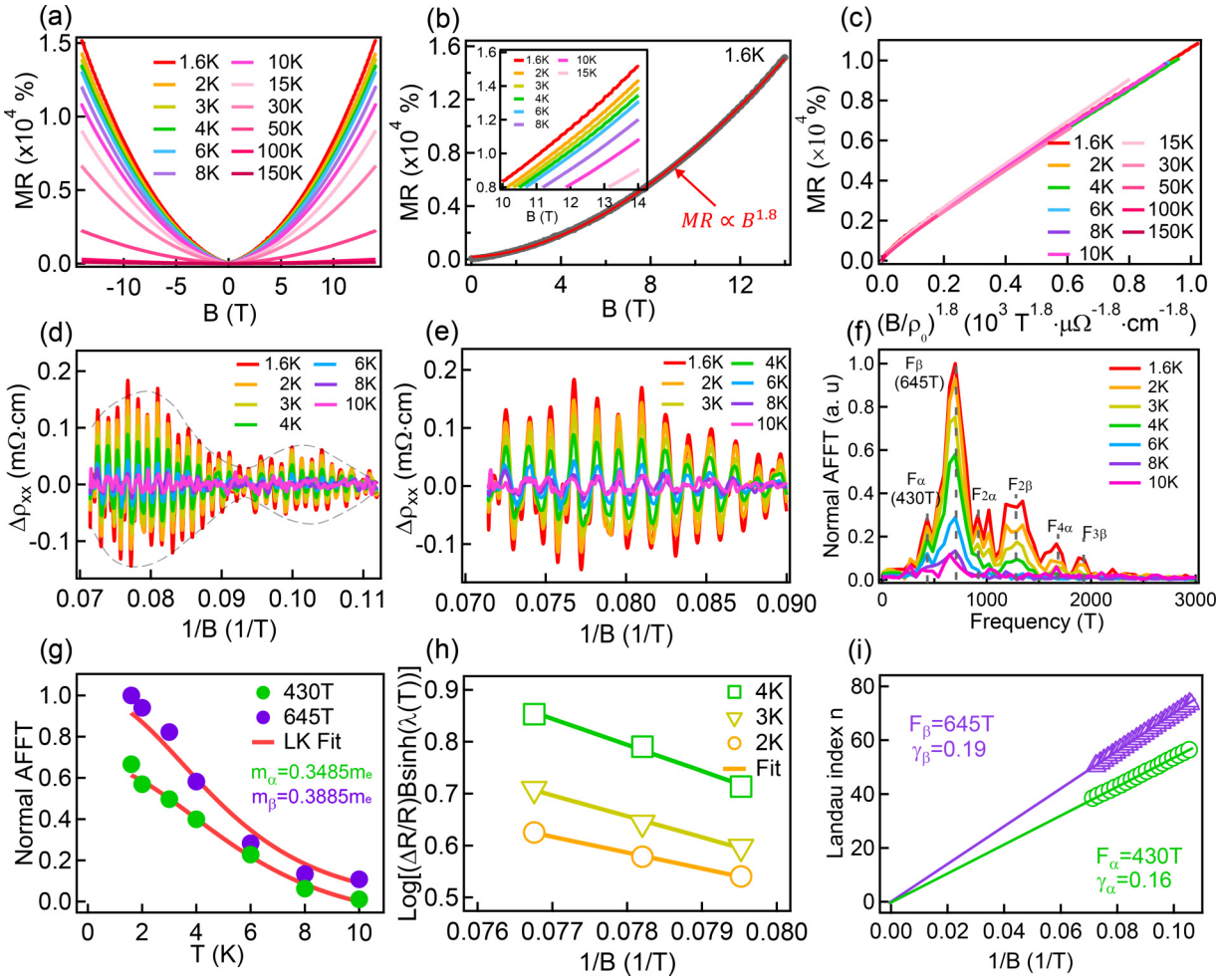

FIG. 3. (a) The field-dependent MR at different temperatures. (b) The MR is fitted by MR $= a + bB^{1.8}$. The inset shows the enlarged view of (a) at high fields. (c) The Kohler plot of the MR from 1.6 to 150 K. All the data follow the same curve of MR $\propto (B/\rho_0)^{1.8}$. (d) The beating pattern of SdH quantum oscillations, extracted by subtracting a smooth background at the temperature from 1.6 to 10 K. (e) The enlarged view of the SdH quantum oscillations in (d) demonstrates that the amplitude decreases as the temperature increases. (f) The FFT amplitude at low temperatures. Two independent oscillation frequencies of 430 (F_α) and 645 T (F_β) can be observed with their higher harmonics. (g) The normalized FFT amplitude as a function of temperature for F_α and F_β, respectively. The red solid lines are the fitted curves with the LK formula. (h) The logarithmic plot at 2, 3, and 4 K. (i) The Landau-level (LL) index fan diagram for F_α and F_β.

To understand that such an MR can be explained by classical theory, Kohler's rule has been considered as

$$\mathrm{MR} \propto (B/\rho_0)^m, \tag{1}$$

where m is a sample-dependent constant that depends on the level of compensation. In Fig. 3(c), the MRs at various temperatures are merged into a single curve when plotted as MR $\sim (B/\rho_0)^{1.8}$ curve; the value is the same as previous reports such as WP_2 [50] and MoO_2 [51], suggesting the validity of Kohler's rule and signifying a universal scattering mechanism at various temperatures. Following Kohler's rule and related argument presented at WTe_2 [43] and other material systems [52], the extremely large MR in our case is attributed to the perfect compensation of electrons and holes, which is also supported by the following theoretical calculations.

In addition, the SdH quantum oscillations with a clear beating pattern have been obtained after subtracting a smooth background at high field and low temperature, as shown in Fig. 3(d). The dashed line is to guide the eyes. The beating SdH quantum oscillations are also observed in the InGaAs/InAlAs two-dimensional electron gas (2DEG) [53,54], the silicon metal oxide 2DEG [55], and the SnTe/Bi_2Te_3 heterostructure [56], in which they are ascribed to the Rashba spin splitting. However, in our case, the Rashba spin splitting is ruled out because there is no interface in our device. Here, these are attributed to two different Fermi surfaces of an electron pocket and a hole pocket, which will be discussed in detail later. Figure 3(e) exhibits the enlarged image from Fig. 3(d). It is seen that the amplitude $\Delta\rho_{xx}$ of the quantum oscillation gradually decreases with temperature increasing until it finally disappears.

In order to obtain more detailed information from the quantum oscillations, fast Fourier transforms (FFTs) of these oscillations are plotted in Fig. 3(f), which reveal two independent frequencies of $F_\alpha = 430$ T and $F_\beta = 645$ T with their higher harmonics of $F_{2\alpha}$, $F_{4\alpha}$ and $F_{2\beta}$, $F_{3\beta}$, respectively. The oscillation frequencies (F) are related to the cross-sectional area (S_F) of the Fermi surface that is normal to the field

TABLE I. The parameters are derived from SdH quantum oscillations, including the SdH quantum oscillation frequency F_α and F_β, the effective mass m^*, the Fermi wave vector k_F, the Fermi level E_F, the Fermi velocity v_F, the quantum scattering time τ, the mobility μ, and the mean-free path ℓ.

	F (T)	m^* (m_e)	k_F (Å^{-1})	E_F (meV)	v_F (10^5 m/s)	τ (10^{-12} s)	μ (cm^2/Vs)	ℓ (nm)
F_α	430	0.3485	0.114	142.2	2.54	1.074	5419	318
F_β	645	0.3885	0.140	192.4	2.95	1.077	4875	273

direction. According to the Onsager relation $F = S_F(\hbar/2\pi e)$, the Fermi-surface areas are $S_F^\alpha = 0.041$ Å^{-2} and $S_F^\beta = 0.062$ Å^{-2}, corresponding to the Fermi wave vector of $k_F^\alpha = 0.114$ Å^{-1} and $k_F^\beta = 0.140$ Å^{-1}, respectively.

Furthermore, the quantum oscillation can be described by the Lifshitz-Kosevich (LK) formula [48],

$$\Delta R/R_0 \propto R_T R_D R_S \cos[2\pi(F/B + \gamma - \delta)], \tag{2}$$

where $R_T = \lambda T/\sinh(\lambda T)$ is the thermal damping factor, $R_D = e^{-D}$ is the Dingle damping factor and $R_S = \cos(g\pi m^*/2m_e)$ is the spin phase factor. Here, $\lambda = 2\pi^2 k_B m^*/\hbar eB$, $D = 2\pi^2 k_B T_D m^*/\hbar eB$, $T_D = \hbar/2\pi k_B \tau$ is the Dingle temperature. The m^*, m_e, $\hbar$, k_B, and g are the effective mass of fermion, the mass of electron, Boltzmann constant, reduced Planck's constant, and g factor, respectively. $\gamma = 1/2 - \Phi_B/2\pi$ is the phase factor and Φ_B is the Berry phase; δ is a phase shift determined by the dimensionality, having values of 0 or $\pm 1/8$ for the 2D or 3D systems, respectively. The thermal damping factor $R_T = \lambda T/\sinh(\lambda T)$ in the LK formula is used to describe the FFT amplitude. As shown in Fig. 3(g), the temperature dependence of the normalized FFT amplitude is well fitted, and the effective masses of $m_\alpha^* = 0.3485\ m_e$ and $m_\beta^* = 0.3885\ m_e$ are extracted, corresponding to $F_\alpha = 430$ T and $F_\beta = 645$ T, respectively. Therefore, the Fermi velocity $v_F = \hbar k_F/m^*$ and the Fermi level $E_F = m^* v_F^2$ are estimated as shown in Table I. According to the LK formula, the quantum scattering time τ is a function of the Dingle temperature T_D, $\tau = \hbar/2\pi k_B T_D$.Thus, the quantum scattering time can be extracted via the logarithmic plot of the log $[(\Delta R/R_0)B\sinh(\lambda T)] \sim K(1/B)$, where the slope $K = 2\pi^2 k_B T_D m^*/\hbar e$, as shown in Fig. 3(h). The quantum scattering time τ can be extracted by using $T_D = \hbar/2\pi k_B \tau$; the value is listed in Table I. Therefore, the mean-free path of the $\ell = v_F \tau$ and mobility $\mu = e\tau/m^*$ can be also estimated [57], and summarized in Table I.

Following the Lifshitz-Onsager quantization rule, $S_F(\hbar/eB) = 2\pi(n + \gamma)$, where n is the Landau-level index (see the Supplemental Material, Fig. S1 for a detailed discussion) [55,56,58]. The nature of the energy band dispersion is determined by the value of the Berry phase Φ_B, which is 0 for the conventional metallic systems with parabolic band dispersion and π for the Dirac-(Weyl-) type systems with a linear band dispersion [47]. In Fig. 3(i), the Landau-level (LL) fan diagrams for $F_\alpha = 430$ T and $F_\beta = 645$ T are plotted, assigning maxima of the SdH quantum oscillation as integers (n) and minimum as half integers ($n + 1/2$). The Berry phase can be extracted from the intercept of the linear extrapolation; the intercepts of $F_\alpha = 430$ T and $F_\beta = 645$ T are extracted as $\gamma_\alpha = 0.16$ and $\gamma_\beta = 0.19$, respectively, which indicates the possible existence of the Dirac-like fermions in the ZrP_2, suggesting that the electronic structure of the ZrP_2 is nontrivial.

Interestingly, the Zeeman splitting is also observed at 1.6 K. As shown in Fig. 4(a), the valleys of the quantum oscillation completely evolve into two subvalleys in the LL index $n = 50.5$, 51.5, 52.5, and 53.5, suggesting the lifting of spin degeneracy due to the Zeeman effect, and the spacing of spin splitting is about 0.0005 T^{-1}. To further investigate the Zeeman splitting, the spin-phase factor $R_S = \cos(g\pi m^*/2m_e)$ is rearranged in the LK formula; thus, the LK formula can be rewritten as

$$\Delta R/R_0 \propto R_T R_D[\cos 2\pi(F/B + \gamma - \delta + \varphi/2) + \cos 2\pi(F/B + \gamma - \delta - \varphi/2)], \tag{3}$$

where the spin-splitting factor $\varphi = gm^*/2m_e$ is the phase difference between spin-up and spin-down electrons. The g factor of 1.2 and 1.7 is obtained with the equation $gm^*/2m_e = F(1/\Delta B)$, corresponding to $F_\alpha = 430$ T and $F_\beta = 645$ T, respectively. The detailed mathematical process and analyses

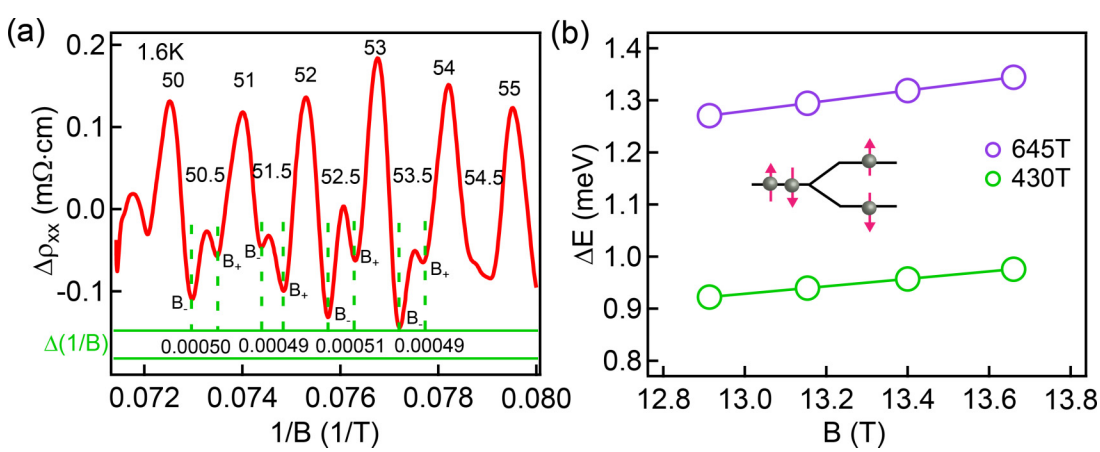

FIG. 4. (a) The SdH quantum oscillation at 1.6 K. (b) The Zeeman energy ΔE as a function of magnetic field B.

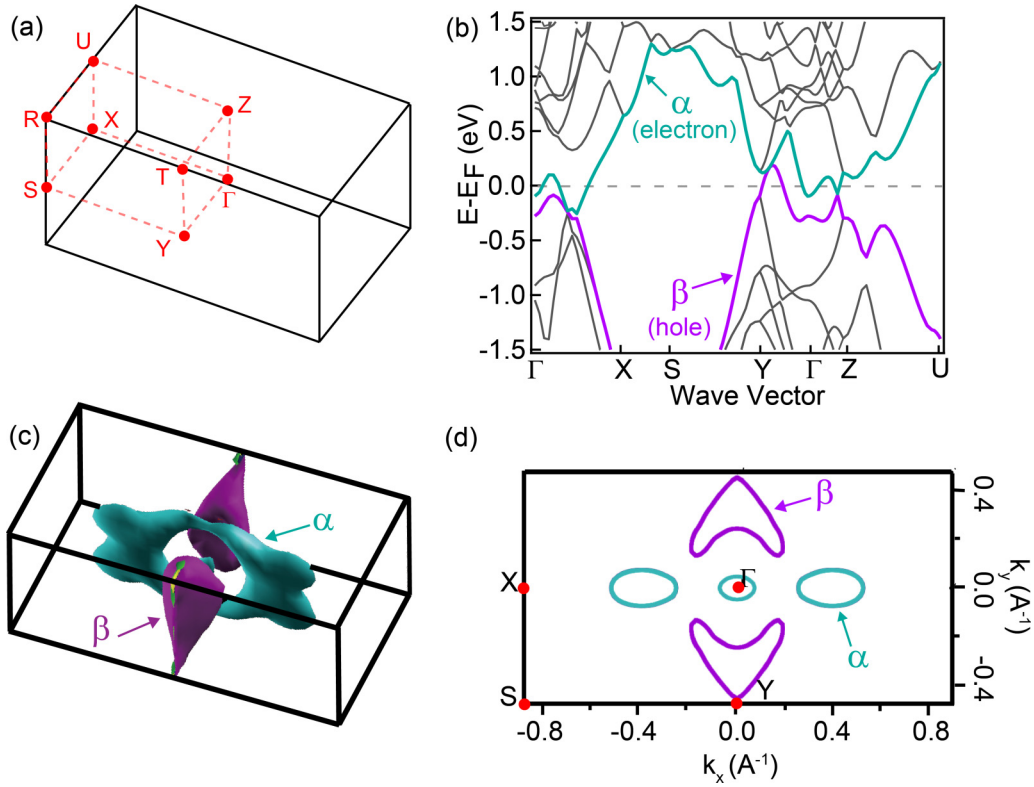

FIG. 5. The electronic structure of ZrP_2 via density-functional theory calculation with spin-orbit coupling. (a) The 3D bulk Brillouin zone of ZrP_2 crystal showing the high-symmetry points and lines. (b) Energy band structures at high-symmetry points and lines. (c) The 3D bulk Fermi surface of ZrP_2, the bands crossing near the Fermi level in (b). (d) The Fermi surface at $k_z = 0$.

are available in previous study [59,60]. The Zeeman splitting energy $\Delta E = g\mu_B B$ of $F_\alpha = 430$ T and $F_\beta = 645$ T is summarized as shown in Fig. 4(b). The Zeeman splitting of the SdH oscillations are also observed in other topological semimetals, such as the Dirac semimetal graphene [61], Cd_3As_2 [62], Weyl semimetal TaP [63], and $ZrTe_5$ [59].

The electronic structure calculations are performed using the density-functional theory calculation with spin-orbit coupling. Figure 5(a) reveals the 3D bulk Brillouin zone of ZrP_2 crystal showing the high-symmetry points and lines. The electronic structure is exhibited in Fig. 5(b). Two band crossings occur near the Fermi level, forming topological Fermi-surface states. The light green and purple represent electron pocket and hole pocket, respectively. Figure 5(c) shows the bulk Fermi surface of ZrP_2 crystal. Fermi surfaces consists of the electron (α) and hole (β) drumhead surface states, which is consistent with the results of the SdH quantum oscillations. Figure 5(d) exhibits the Fermi surface at $k_z = 0$; the cross-sectional areas of electron (α) and hole (β) pockets are obtained ($S^\alpha = 0.045$ Å^{-2} and $S^\beta = 0.062$ Å^{-2}), which is also consistent with the results extracted from the SdH oscillations ($S_F^\alpha = 0.041$ Å^{-2} and $S_F^\beta = 0.062$ Å^{-2}).

IV. CONCLUSION

In summary, we report the single-crystal growth and magnetotransport properties of the possible nodal-line semimetal ZrP_2. A magnetic-field induced metal-to-insulator transition and a resistivity plateau are observed at low temperatures. An extremely large MR of 10^4% is obtained, which is attributed to the electron-hole compensation. The beating pattern in the SdH quantum oscillation is also observed below 10 K, which mainly stems from the superposition of the quantum oscillations of the electron and hole pockets, which is consistent with the theoretical calculation results. Besides, the valley of SdH quantum oscillation is split into two subvalleys due to Zeeman effect at 1.6 K. This study is meaningful for future investigations of topological semimetals and condensed-matter physics.

ACKNOWLEDGMENTS

The paper is supported by the National Natural Science Foundation of China (Grants No. 12241403 and No. 61974061) and the Natural Science Foundation of Jiangsu Province of China (Grant No. BK20140054).

[1] S.-Y. Xu, I. Belopolski, N. Alidoust, M. Neupane, G. Bian, C. L. Zhang, R. Sankar, G. Q. Chang, Z. j. Yuan, C.-C. Lee, S.-M. Huang, H. Zheng, J. Ma, D. S. Sanchez, B. K. Wang, A. Bansil, F. C. Chou, P. P. Shibayev, H. Lin, S. Jia, and M. Z. Hasan, Discovery of a Weyl fermion semimetal and topological Fermi arcs, Science **349**, 613 (2015).

[2] Z. K. Liu, B. Zhou, Y. Zhang, Z. J. Wang, H. M. Weng, D. Prabhakaran, S.-K. Mo, Z. X. Shen, Z. Fang, X. Dai, Z. Hussain, and Y. L. Chen, Discovery of a three-dimensional topological Dirac semimetal, Na_3Bi, Science **343**, 864 (2014).

[3] C. Shekhar, A. K. Nayak, Y. Sun, M. Schmidt, M. Nicklas, I. Leermakers, U. Zeitler, Y. Skourski, J. C. Wosnitza, Z. K. Liu, Y. L. Chen, W. Schnelle, H. Borrmann, Y. Grin, C. Felser, and B. H. Yan, Extremely large magnetoresistance and ultrahigh mobility in the topological Weyl semimetal candidate NbP, Nat. Phys. **11**, 645 (2015).

[4] M. N. Ali, J. Xiong, S. Flynn, J. Tao, Q. D. Gibson, L. M. Schoop, T. Liang, N. Haldolaarachchige, M. Hirschberger, N. P. Ong, and R. J. Cava, Large, non-saturating magnetoresistance in WTe_2, Nature (London) **514**, 205 (2014).

[5] J. Bannies, E. Razzoli, M. Michiardi, H. H. Kung, I. S. Elfimov, M. Yao, A. Fedorov, J. Fink, C. Jozwiak, A. Bostwick, E. Rotenberg, A. Damascelli, and C. Felser, Extremely large magnetoresistance from electron-hole compensation in the nodal-loop semimetal ZrP_2, Phys. Rev. B **103**, 155144 (2021).

[6] T. Liang, Q. Gibson, M. N. Ali, M. Liu, R. J. Cava, and N. P. Ong, Ultrahigh mobility and giant magnetoresistance in the Dirac semimetal Cd_3As_2, Nat. Mater. **14**, 280 (2015).

[7] Z. Wang, Y. Zheng, Z. Shen, Y. Lu, H. Fang, F. Sheng, Y. Zhou, X. Yang, Y. Li, C. Feng, and Z.-A. Xu, Helicity-protected ultrahigh mobility Weyl fermions in NbP, Phys. Rev. B **93**, 121112(R) (2016).

[8] D. S. Wu, J. Liao, W. Yi, X. Wang, P. G. Li, H. M. Weng, Y. G. Shi, Y. Q. Li, J. L. Luo, X. Dai, and Z. Fang, Giant semiclassical magnetoresistance in high mobility $TaAs_2$ semimetal, Appl. Phys. Lett. **108**, 042105 (2016).

[9] F. D. Tang, Y. F. Ren, P. P. Wang, R. D. Zhong, J. Schneeloch, S. Y. A. Yang, K. Yang, P. A. Lee, G. D. Gu, Z. H. Qiao, and L. Y. Zhang, Three-dimensional quantum Hall effect and metal-insulator transition in $ZrTe_5$, Nature (London) **569**, 537 (2019).

[10] C. Zhang, Y. Zhang, X. Yuan, S. Lu, J. Zhang, A. Narayan, Y. Liu, H. Zhang, Z. Ni, R. Liu, E. S. Choi, A. Suslov, S. Sanvito, L. Pi, H. Z. Lu, A. C. Potter, and F. X. Xiu, Quantum Hall effect based on Weyl orbits in Cd_3As_2, Nature (London) **565**, 331 (2019).

[11] D. -X. Qu, Y. S. Hor, J. Xiong, R. J. Cava, and N. P. Ong, Quantum oscillations and Hall anomaly of surface states in Bi_2Te_3, Science **329**, 821 (2010).

[12] N. P. Armitage, E. J. Mele, and A. Vishwanath, Weyl and Dirac semimetals in three-dimensional solids, Rev. Mod. Phys. **90**, 015001 (2018).

[13] J. Hu, S. -Y. Xu, N. Ni, and Z. Q. Mao, Transport of topological semimetals, Annu. Rev. Mater. Res. **49**, 207 (2019).

[14] B. Q. Lv, T. Qian, and H. Ding, Experimental perspective on three-dimensional topological semimetals, Rev. Mod. Phys. **93**, 025002 (2021).

[15] Z. K. Liu, J. Jiang, B. Zhou, Z. J. Wang, Y. Zhang, H. M. Weng, D. Prabhakaran, S. K. Mo, H. Peng, P. Dudin, T. Kim, M. Hoesch, Z. Fang, X. Dai, Z. X. Shen, D. L. Feng, Z. Hussain, and Y. L. Chen, A stable three-dimensional topological Dirac semimetal Cd_3As_2, Nat. Mater. **13**, 677 (2014).

[16] B. Q. Lv, N. Xu, H. M. Weng, J. Z. Ma, P. Richard, X. C. Huang, L. X. Zhao, G. F. Chen, C. E. Matt, F. Bisti, V. N. Strocov, J. Mesot, Z. Fang, X. Dai, T. Qian, M. Shi, and H. Ding, Observation of Weyl nodes in TaAs, Nat. Phys. **11**, 724 (2015).

[17] J. Xiong, S. K. Kushwaha, T. Liang, J. W. Krizan, M. Hirschberger, W. D. Wang, R. J. Cava, J. W. Krizan, and N. P. Ong, Evidence for the chiral anomaly in the Dirac semimetal Na_3Bi, Science **350**, 413 (2015).

[18] F. Arnold, C. Shekhar, S. C. Wu, Y. Sun, R. D. Dos Reis, N. Kumar, M. Naumann, M. O. Ajeesh, M. Schmidt, A. G. Grushin, J. H. Bardarson, M. Baenitz, D. Sokolov, H. Borrmann, M. Nicklas, C. Felser, E. Hassinger, and B. H. Yan, Negative magnetoresistance without well-defined chirality in the Weyl semimetal TaP, Nat. Commun. **7**, 11615 (2016).

[19] X. Huang, L. Zhao, Y. Long, P. Wang, D. Chen, Z. Yang, H. Liang, M. Xue, H. Weng, Z. Fang, X. Dai, and G. Chen, Observation of the chiral-anomaly-induced negative magnetoresistance in 3D Weyl semimetal TaAs, Phys. Rev. X **5**, 031023 (2015).

[20] N. Kumar, Y. Sun, N. Xu, K. Manna, M. Yao, V. Suss, I. Leermakers, O. Young, T. Forster, M. Schmidt, H. Borrmann, B. Yan, U. Zeitler, M. Shi, C. Felser, and C. Shekhar, Extremely high magnetoresistance and conductivity in the type-II Weyl semimetals WP_2 and MoP_2, Nat. Commun. **8**, 1642 (2017).

[21] W. Zhou, J. Chen, H. Gao, T. Hu, S. Ruan, A. Stroppa, and W. Ren, Anomalous and polarization-sensitive photoresponse of Td-WTe_2 from visible to infrared light, Adv. Mater. **31**, 1804629 (2019).

[22] K. Zhang, X. Fang, Y. Wang, Y. Wan, Q. Song, W. Zhai, Y. Li, G. Ran, Y. Ye, and L. Dai, Ultrasensitive near-infrared photodetectors Based on a graphene-MoTe2-graphene vertical van der Waals heterostructure, ACS Appl. Mater. Interfaces **9**, 6 (2017).

[23] T. Wu, Q. Qiu, Y. Li, Q. Zhou, W. Ma, J. Li, L. Jiang, W. Zhou, and Z. Huang, High sensitivity of semimetal photodetection via Bose–Einstein condensation, InfoMat **6**, 2 (2024).

[24] Z.-M. Wei and J.-B. Xia, Recent progress in polarization-sensitive photodetectors based on low-dimensional semiconductors, Acta Phys. Sin. **68**, 16 (2019).

[25] Q. Wang, J. Zheng, Y. He, J. Cao, X. Liu, M. Wang, J. Ma, J. Lai, H. Lu, S. Jia, D. Yan, Y. Shi, J. Duan, J. Han, W. Xiao, J.-H. Chen, K. Sun, Y. Yao, and D. Sun, Robust edge photocurrent response on layered type II Weyl semimetal WTe_2, Nat. Commun. **10**, 5736 (2019).

[26] S. Verma, R. Yadav, A. Pandey, M. Kaur, and S. Husale, Investigating active area dependent high performing photoresponse through thin films of Weyl semimetal WTe_2, Sci. Rep. **13**, 197 (2023).

[27] G. B. Osterhoudt, L. K. Diebel, M. J. Gray, X. Yang, J. Stanco, X. Huang, B. Shen, N. Ni, P. J. W. Moll, Y. Ran, and K. S. Burch, Colossal mid-infrared bulk photovoltaic effect in a type-I Weyl semimetal, Nat. Mater. **18**, 5 (2019).

[28] W. Lu, Z. Fan, Y. Yang, J. Ma, J. Lai, X. Song, X. Zhuo, Z. Xu, J. Liu, X. Hu, S. Zhou, F. Xiu, J. Cheng, and D. Sun, Ultrafast photothermoelectric effect in Dirac semimetallic Cd_3As_2 revealed by terahertz emission, Nat. Commun. **13**, 1623 (2022).

[29] M. Hemmat, S. Ayari, M. Mičica, H. Vergnet, S. Guo, M. Arfaoui, X. Yu, D. Vala, A. Wright, K. Postava, J. Mangeney, F. Carosella, S. Jaziri, Q. J. Wang, Z. Liu, J. Tignon, R. Ferreira, E. Baudin, and S. Dhillon, Layer-controlled nonlinear terahertz valleytronics in two-dimensional semimetal and semiconductor $PtSe_2$, InfoMat **5**, 11 (2023).

[30] Y. Gao, S. Kaushik, E. J. Philip, Z. Li, Y. Qin, Y. P. Liu, W. L. Zhang, Y. L. Su, X. Chen, H. Weng, D. E. Kharzeev, M. K. Liu, and J. Qi, Chiral terahertz wave emission from the Weyl semimetal TaAs, Nat. Commun. **11**, 720 (2022).

[31] Q. Xu, R. Yu, Z. Fang, X. Dai, and H. Weng, Topological nodal line semimetals in the CaP_3 family of materials, Phys. Rev. B **95**, 045136 (2017).

[32] J. Hu, Z. Tang, J. Liu, X. Liu, Y. Zhu, D. Graf, K. Myhro, S. Tran, C. N. Lau, J. Wei, and Z. Mao, Evidence of topological nodal-line fermions in ZrSiSe and ZrSiTe, Phys. Rev. Lett. **117**, 016602 (2016).

[33] J. Hu, X. Liu, C. L. Yue, J. Y. Liu, H. W. Zhu, J. B. He, J. Wei, Z. Q. Mao, L. Y. Antipina, Z. I. Popov, P. B. Sorokin, T. J. Liu, P. W. Adams, S. M. A. Radmanesh, L. Spinu, H. Ji, and D. Natelson, Enhanced electron coherence in atomically thin Nb_3SiTe_6, Nat. Phys. **11**, 471 (2015).

[34] C. Sims, M. M. Hosen, H. Aramberri, C. -Y. Huang, G. Dhakal, K. Dimitri, F. Kabir, S. Regmi, X. Zhou, T.-R. Chang, H. Lin, D. Kaczorowski, N. Kioussis, and M. Neupane, Termination-dependent topological surface states in nodal-loop semimetal HfP_2, Phys. Rev. Mater. **4**, 054201 (2020).

[35] J. Ma, Q. Gu, Y. Liu, J. Lai, P. Yu, X. Zhuo, Z. Liu, J.-H. Chen, J. Feng, and D. Sun, Nonlinear photoresponse of type-II Weyl semimetals, Nat. Mater. **18**, 5 (2019).

[36] M. Huber and H. J. Deiseroth, Crystal structure of zirconium diphosphide, ZrP_2, Z. Kristallogr. **209**, 370 (1994).

[37] F. Hulliger, New representives of the $NbAs_2$ and $ZrAs_2$ structures, Nature (London) **204**, 775 (1964).

[38] X. C. Yang, X. Luo, J. J. Gao, Z. Z. Jiang, W. Wang, T. Y. Wang, J. G. Si, C. Y. Xi, W. H. Song, and Y. P. Sun, Planar Hall effect in the quasi-one-dimensional topological superconductor $TaSe_3$, Phys. Rev. B **104**, 155106 (2021).

[39] L. He, F. Xiu, Y. Wang, A. V. Fedorov, G. Huang, X. Kou, M. Lang, W. P. Beyermann, J. Zou, and K. L. Wang, Epitaxial growth of Bi_2Se_3 topological insulator thin films on Si (111), J. Appl. Phys. **109**, 103702 (2011).

[40] L. He, F. Xiu, X. Yu, M. Teague, W. Jiang, Y. Fan, X. Kou, M. Lang, Y. Wang, G. Huang, N. C. Yeh, and K. L. Wang, Surface-dominated conduction in a 6 nm thick Bi_2Se_3 thin film, Nano Lett. **12**, 3 (2012).

[41] D. J. Kim, J. Xia, and Z. Fisk, Topological surface state in the Kondo insulator samarium hexaboride, Nat. Mater. **13**, 466 (2014).

[42] F. F. Tafti, Q. D. Gibson, S. K. Kushwaha, N. Haldolaarachchige, and R. J. Cava, Resistivity plateau and extreme magnetoresistance in LaSb, Nat. Phys. **12**, 272 (2015).

[43] Y. L. Wang, L. R. Thoutam, Z. L. Xiao, J. Hu, S. Das, Z. Q. Mao, J. Wei, R. Divan, A. Luican-Mayer, G. W. Crabtree, and W. K. Kwok, Origin of the turn-on temperature behavior in WTe_2, Phys. Rev. B **92**, 180402(R) (2015).

[44] Y.-Y. Wang, Q.-H. Yu, P.-J. Guo, K. Liu, and T.-L. Xia, Resistivity plateau and extremely large magnetoresistance in $NbAs_2$ and TaAs2, Phys. Rev. B **94**, 041103(R) (2016).

[45] D. V. Khveshchenko, Magnetic-field-induced insulating behavior in highly oriented pyrolitic graphite, Phys. Rev. Lett. **87**, 206401 (2001).

[46] Y. Kopelevich, J. C. M. Pantoja, R. R. da Silva, and S. Moehlecke, Universal magnetic-field-driven metal-insulator-metal transformations in graphite and bismuth, Phys. Rev. B **73**, 165128 (2006).

[47] R. Singha, A. K. Pariari, B. Satpati, and P. Mandal, Large nonsaturating magnetoresistance and signature of nondegenerate Dirac nodes in ZrSiS, Proc. Natl Acad. Sci. **114**, 2468 (2017).

[48] L. Guo, T.-W. Chen, C. Chen, L. Chen, Y. Zhang, G.-Y. Gao, J. Yang, X.-G. Li, W.-Y. Zhao, S. Dong, and R.-K. Zheng, Electronic transport evidence for topological nodal-line semimetals of ZrGeSe single crystals, ACS Appl. Electron. Mater. **1**, 869 (2019).

[49] Y. Li, L. Li, J. Wang, T. Wang, X. Xu, C. Xi, C. Cao, and J. Dai, Resistivity plateau and negative magnetoresistance in the topological semimetal $TaSb_2$, Phys. Rev. B **94**, 121115(R) (2016).

[50] J. Du, Z. Lou, S. Zhang, Y. Zhou, B. Xu, Q. Chen, Y. Tang, S. Chen, H. Chen, Q. Zhu, H. Wang, J. Yang, Q. Wu, O. V. Yazyev, and M. Fang, Extremely large magnetoresistance in the topologically trivial semimetal α-WP_2, Phys. Rev. B **97**, 245101 (2018).

[51] Q. Chen, Z. Lou, S. Zhang, B. Xu, Y. Zhou, H. Chen, S. Chen, J. Du, H. Wang, J. Yang, Q. Wu, O. V. Yazyev, and M. Fang, Large magnetoresistance and nonzero Berry phase in the nodal-line semimetal MoO_2, Phys. Rev. B **102**, 165133 (2020).

[52] J. Xu, F. Han, T.-T. Wang, L. R. Thoutam, S. E. Pate, M. D. Li, X. F. Zhang, Y.-L. Wang, R. Fotovat, U. Welp, X. Q. Zhou, W.-K. Kwok, D. Y. Chung, M. G. Kanatzidis, and Z.-L. Xiao, Extended Kohler's rule of magnetoresistance, Phys. Rev. X **11**, 041029 (2021).

[53] C. L. Yang, H. T. He, L. Ding, L. J. Cui, Y. P. Zeng, J. N. Wang, and W. K. Ge, Spectral dependence of spin photocurrent and current-induced spin polarization in an InGaAs/InAlAs two-dimensional electron gas, Phys. Rev. Lett. **96**, 186605 (2006).

[54] L. J. Cui, Y. P. Zeng, Y. Zhang, W. Z. Zhou, L. Y. Shang, T. Lin, and J. H. Chu, Beating patterns in the Shubnikov-de Haas oscillations originated from spin splitting in In0.52Al0.48As/In0.65Ga0.35As heterostructures: Experiment and calculation, Physica E **83**, 114 (2016).

[55] M. Lodari, L. Lampert, O. Zietz, R. Pillarisetty, J. S. Clarke, and G. Scappucci, Valley splitting in silicon from the interference pattern of quantum oscillations, Phys. Rev. Lett. **128**, 176603 (2022).

[56] A. K. Okazaki, S. Wiedmann, S. Pezzini, M. L. Peres, P. H. O. Rappl, and E. Abramof, Shubnikov-de Haas oscillations in topological crystalline insulator SnTe(111) epitaxial films, Phys. Rev. B **98**, 195136 (2018).

[57] P. Li, Y. Wen, X. He, Q. Zhang, C. Xia, Z.-M. Yu, S. A. Yang, Z. Zhu, H. N. Alshareef, and X.-X. Zhang, Evidence for topological type-II Weyl semimetal WTe_2, Nat. Commun. **8**, 2150 (2017).

[58] See Supplemental Material at http://link.aps.org/supplemental/10.1103/PhysRevB.109.165155 for the fitting of SdH quantum oscillations and their components using the LK formula at 1.6 K.

[59] Y. Liu, X. Yuan, C. Zhang, Z. Jin, A. Narayan, C. Luo, Z. Chen, L. Yang, J. Zou, X. Wu, S. Sanvito, Z. Xia, L. Li, Z. Wang, and F. Xiu, Zeeman splitting and dynamical mass generation in Dirac semimetal $ZrTe_5$, Nat. Commun. **7**, 12516 (2016).

[60] A. Narayanan, M. D. Watson, S. F. Blake, N. Bruyant, L. Drigo, Y. L. Chen, D. Prabhakaran, B. Yan, C. Felser, T. Kong, P. C. Canfield, and A. I. Coldea, Linear magnetoresistance caused by mobility fluctuations in *n*-doped Cd_3As_2, Phys. Rev. Lett. **114**, 117201 (2015).

[61] Y. J. Song, A. F. Otte, Y. Kuk, Y. Hu, D. B. Torrance, P. N. First, W. A. de Heer, H. Min, S. Adam, M. D. Stiles, A. H. MacDonald, and J. A. Stroscio, High-resolution tunnelling spectroscopy of a graphene quartet, Nature (London) **467**, 185 (2010).

[62] J. Cao, S. Liang, C. Zhang, Y. Liu, J. Huang, Z. Jin, Z. G. Chen, Z. Wang, Q. Wang, J. Zhao, S. Li, X. Dai, J. Zou, Z. Xia, L. Li, and F. Xiu, Landau level splitting in Cd_3As_2 under high magnetic fields, Nat. Commun. **6**, 7779 (2015).

[63] J. Hu, J. Y. Liu, D. Graf, S. M. Radmanesh, D. J. Adams, A. Chuang, Y. Wang, I. Chiorescu, J. Wei, L. Spinu, and Z. Q. Mao, π Berry phase and Zeeman splitting of Weyl semimetal TaP, Sci. Rep. **6**, 18674 (2016).